Science Advances

AAAS

advances.sciencemag.org/cgi/content/full/2/6/e1600417/DC1

Supplementary Materials for

Mimosa Origami: A nanostructure-enabled directional self-organization regime of materials

William S. Y. Wong, Minfei Li, David R. Nisbet, Vincent S. J. Craig, Zuankai Wang, Antonio Tricoli

Published 24 June 2016, *Sci. Adv.* **2**, e1600417 (2016)
DOI: 10.1126/sciadv.1600417

The PDF file includes:

- table. S2. Material properties of Janus bilayers.
- Legends for movies S1 to S9
- References (*37–44*)

Other Supplementary Material for this manuscript includes the following:
(available at advances.sciencemag.org/cgi/content/full/2/6/e1600417/DC1)

- movie S1 (.mp4 format). Static self-assembling properties of circular-shaped Janus bilayer demonstrating artificial tropism in response to a microdroplet.
- movie S2 (.mp4 format). Mimosa Origami assembly of the Janus bilayer strips on a superhydrophobic PS-PDMS substrate.
- movie S3 (.mp4 format). Mimosa Origami assembly of the Janus bilayer strips performing double right-angle turns on a superhydrophobic PS-PDMS substrate.
- movie S4 (.mp4 format). Mimosa Origami assembly of the Janus bilayer strips performing longer and tighter double right-angle turns on a superhydrophobic PS-PDMS substrate.
- movie S5 (.mp4 format). Mimosa Origami assembly of the Janus bilayer strips on a superhydrophobic PS-PDMS substrate.
- movie S6 (.mp4 format). Modular microfluidics: Janus-based Mimosa Origami strips with double-ended bulbs on a superhydrophobic PS-PDMS substrate showing in-channel droplet mixing.
- movie S7 (.mp4 format). Modular microfluidics: Janus-based Mimosa Origami strips with double-ended bulbs, with a central bulb on a superhydrophobic PS-PDMS substrate, showing in-bulb droplet mixing.
- movie S8 (.mp4 format). Modular microfluidics: Janus-based Mimosa Origami strips at a T-junction, showcasing double-ended split for potential in multichannel capabilities.
- movie S9 (.mp4 format). Cyclic insertion and removal of water from an as-assembled microfluidics channel, showcasing suitability toward pump-aided microfluidic designs.

Supplementary Text

Wetting properties of the PCL layer

Notably, the PCL-side of the Janus bilayers was not instantaneously superhydrophilic (*37*). Its contact angle with water was initially 33° and gradually reached 0° in ca. 40 s (fig. S4). This was attributed to the gradual wicking of water through its porous fibrous interface. This unique droplet-interface regime has been previously coined as the sunny-side up state (*38*). In such materials, the penetration front exceeds the contact radius and wicking-induced wetting is accounted to hydrodynamic effects (*38, 39*). While the hemi-wicking effect is well-studied through the Washburn equation (*14*) and was also recently modeled using experiments with regular micropillar forests (*38, 39*), its application for the self-assembling of soft materials remains unprecedented (*40*).

Static self-assembly of the Janus bilayers

While the static self-assembly of thin flat solid films by elasto-capillary has been demonstrated and described by Gao and McCarthy (*31*), and McHale (*16*), the cascade directional self-assembly of the Mimosa Origami effect presented here is unprecedented. A comparison with the previously reported elasto-capillary folding of flat films was pursued by shaping the Janus bilayer into a circular shape with a diameter of 10 mm (fig. S6). Upon contact of the PCL side with a water droplet, the Janus bilayer folds violently, while wetting of the superhydrophobic PVC side yields no response. This is attributed to the very high surface roughness (r = 68) and total surface energy of nanofiber-based PCL layer. This can significantly enhance the surface energy gradient driving the folding of the Janus bilayer during its local wetting above that of dense polymer films. In dense flat films, elasto-capillary bending is driven by reduction of the overall surface energy whereby the vapor-liquid interface is replaced with the liquid-solid interface (*16*). However, for a superhydrophobic porous surface such as the PVC side of the Janus bilayer, the water droplet contacts only a fraction of the solid surface. As a result, the surface energy reduction driving the folding of the PVC side is dramatically reduced. In contrast, the swift clamping

motion of the of the hydrophilic PCL rough interface around a droplet is extremely rapid (*16*, *29*, *31*) due to the higher total surface energy of the porous nanofiber layer than that of a dense flat hydrophilic film. As discussed, in the theoretical model (Fig. 3C and Supplementary Calculations below), this high surface energy of the Janus bilayer PCL side is critical in decreasing the minimal folding width of the folding strip and enabling the cascade propagation of the Mimosa Origami self-assembly.

To investigate the role of surface energy on the Mimosa Origami effect, a superhydrophilic PCL side Janus bilayer was subsequently produced by exposing a disc cutout of the bilayer to water vapor plasma (50 W, 3 mins). This superhydrophilic/superhydrophobic Janus bilayer also demonstrated a strong and rapid water-induced folding. However, upon these initial trials, the plasma-induced superhydrophilic PCL interface was not further considered due to complete infiltration (wet-through) and its inherent lack of longevity (ease of contamination by airborne organics). In contrast, the hemi-wicking/superhydrophobic Janus bilayers perfectly preserved desirable functional properties for extended periods (tested up to 6 months).

Role of substrate and bilayer composition on self-assembly dynamics during Mimosa Origami

Two key properties are required for the optimal dynamic self-assembly during Mimosa Origami. Firstly, the nanofibrous hemiwicking PCL layer requires a super-hydrophobic backbone. PCL monolayers suffer from rapid wet-through failure during utilization. This limits the capability of imparting a directionality to the self-assembly process and result in an inefficient conversion of chemical into kinetic energy. This was exemplified by the comparative analysis of Mimosa Origami self-assembly of PCL monolayers and Janus bilayers on both paper and superhydrophobic dewetting substrates. On the paper substrates, PCL monolayers with a strip widths of 2 and 3 mm experienced catastrophic failures (fig. S8C-D), by wet-through driven pinning to the substrate and uncontrolled in-plane wrinkling. Contrastingly, the Janus bilayers retained complete functionality even on these paper (hydrophilic) substrates (fig. S8A-B) and

dynamically self-assembled into micro-channels. However, the use of a PDMS-PS superhydrophobic substrate enabled much better performance. Even the PCL monolayer variant was capable of some partially directional self-organization (fig. S12). Nevertheless, the performance of the PCL monolayer was suboptimal and suffered from inevitable wet-through failure after a short self-assembly distance. Secondly, the free-motion of the Janus bilayers is required for dynamical self-assembly to occur. Binding the Janus bilayers onto a sticky substrate physically hinders the self-assembly, which then prevents folding signal propagation. As a result, cascading-dependent Mimosa Orgami becomes impossible on plain PDMS substrates.

Supplementary Calculations

Energy density of hemi-wicking PCL films

The energy density (u, Jkg^{-1}) of the hemi-wicking PCL nanofiber layer was computed from its material and surface properties as

$$u = \frac{1}{m} [\pi D h \gamma_{LV} cos(\theta_e)] \quad \text{(S1)}$$

where, m is the PCL layer mass in kg, D is the average nanofiber diameter (m), h is the specific nanofiber length (mkg^{-1}), γ_{LV} is the surface energy density of water (0.072 Nm^{-1}) and θ_e is the characteristic contact angle.

The D is 192 ± 49 nm as measured by SEM. The θ_e is 81.9 ± 1.9° as averaged by static CAs measurements determined through 5 repeats on a quasi-flat interface of PCL fabricated by spin-coating. The measured CAs were 83.24°, 82.25°, 81.93°, 83.37°, 78.64° and in line with the literature (*41*).

Based on the density of PCL of 1145 kgm^{-3}, the specific length (h, mkg^{-1}) of the PCL layer was computed as

$$h = \frac{4}{\pi \rho (D^2)} \quad \text{(S2)}$$

Through Equation S2, the specific length (h) was computed at 3.02 x 10^{10} mkg^{-1}. Inserting known values into Equation S1 gave the final energy density of the material, which was notably enhanced through the ultra-high surface area conferred by the nanofibrous nature of the material

$$u = 185\, Jkg^{-1}$$

Roughness ratio analysis of PCL nanofibers (Gravimetric and SEM)

The roughness (r) of the nanofibrous PCL layer was computed from the ratio of the total surface area of the PCL layer to the geometric surface area

$$r = \frac{4m\varnothing}{\pi \rho D^2} \quad \text{(S3)}$$

where m is the mass (3.74×10^{-3} kgm^{-2}) of the monolayer PCL per cm^2, $\varnothing$ is the average circumference of a nanofiber (601×10^{-9} m), ρ is the density of PCL (1145 kgm^{-3}), D is the average diameter of a nanofiber (192×10^{-9} m). Inserting these values into S3 results in a r of 67.8.

Supplementary Material Data

Self-assembled micro-channels and dimensions

The diameters of the self-assembled micro-channels were measured from photographic images and reported in table S1.

table S1. Width-to-diameter ratios of Mimosa Origami–assembled microchannels.

Janus Bilayer Strip Width (μm)	Assembled 3D Channel Diameter (μm)	Strip Width to Diameter Ratio
2000	490	4.08
3000	1050	2.86
4000	1720	2.33
5000	2700	1.85

Ideal self-assembly of cylindrical geometries from flat rectangles comprises of a width: diameter ratio of π. Values higher than π would have achieved idealized cylindrical folding (with some overlap) while values lower than π would have had folded into a suboptimal flattened cylinder.

Material analysis of PCL-PVC Janus bilayers by DMA and WLI

The thickness of the Janus bilayer (on PDMS) was measured by white light interferometry (WLI). The Janus bilayer's Young's Modulus was measured through stress-strain curves with a dynamical

mechanical analyzer (DMA8000, PerkinElmer, USA). The Poisson's ratio was assumed at 0.47, in line with previous studies (*42*, *43*).

table S2. Material properties of Janus bilayers.

Young's Modulus (*E*) - DMA	4.85 MPa
Poisson's ratio (*v*) (*42*, *43*)	0.47 (*43*)
Film thickness (*h*) - WLI	51 µm

Supplementary Equations

McHale critical droplet size

$$L_{EC} = \frac{K_b}{\gamma_{LV}} \tag{S4}$$

$$K_b = \frac{Eh^3}{12(1-v)} \tag{S5}$$

where K_b is the bending rigidity, γ_{LV} is the surface energy density of water (0.072 Nm^{-1}), and E and v are the Young's Modulus and Poisson's ratio for the material.

Lucas-Washburn Rideal equation

$$x = \sqrt{\left(\frac{r\gamma}{\eta}\frac{\cos(\theta)}{2}\right)t} \tag{S6}$$

where x is the displacement (m), r is the radius of the capillary (m), γ is the surface tension of water (0.072 Nm^{-1}), θ is the apparent contact angle (°), t is the time (s) and η is the dynamic viscosity (1 mPa s^{-1}).

Laplace pressure in a capillary

$$\Delta P = \frac{2\gamma}{r} \quad \text{(S7)}$$

where ΔP is the Laplace pressure (Pa), γ is the surface tension of water (0.072 Nm^{-1}) and r is the radius of the capillary (m).

Solid surface energy estimation from contact angle

$$\gamma_{SV} \approx \gamma_{LV} \left(\frac{(1+\cos\theta_e)^2}{4\Phi^2}\right) \quad \text{(S8)}$$

where γ_{SV} is the surface energy density of the solid, γ_{LV} is the surface energy density of water (0.072 Nm^{-1}), θ_e is the characteristic contact angle, Φ is the ratio involving the free energies of adhesion and cohesion for two phases (*44*)

$$\Phi = \frac{4(V_s V_l)^{1/3}}{(V_s^{1/3} V_l^{1/3})^2} \quad \text{(S9)}$$

where $V_{s/l}$ represents the molar volume, computed as $V_{s/l} = M/\rho$ where M is the molar mass ($kgmol^{-1}$), and ρ is density of the material (kgm^{-3}).

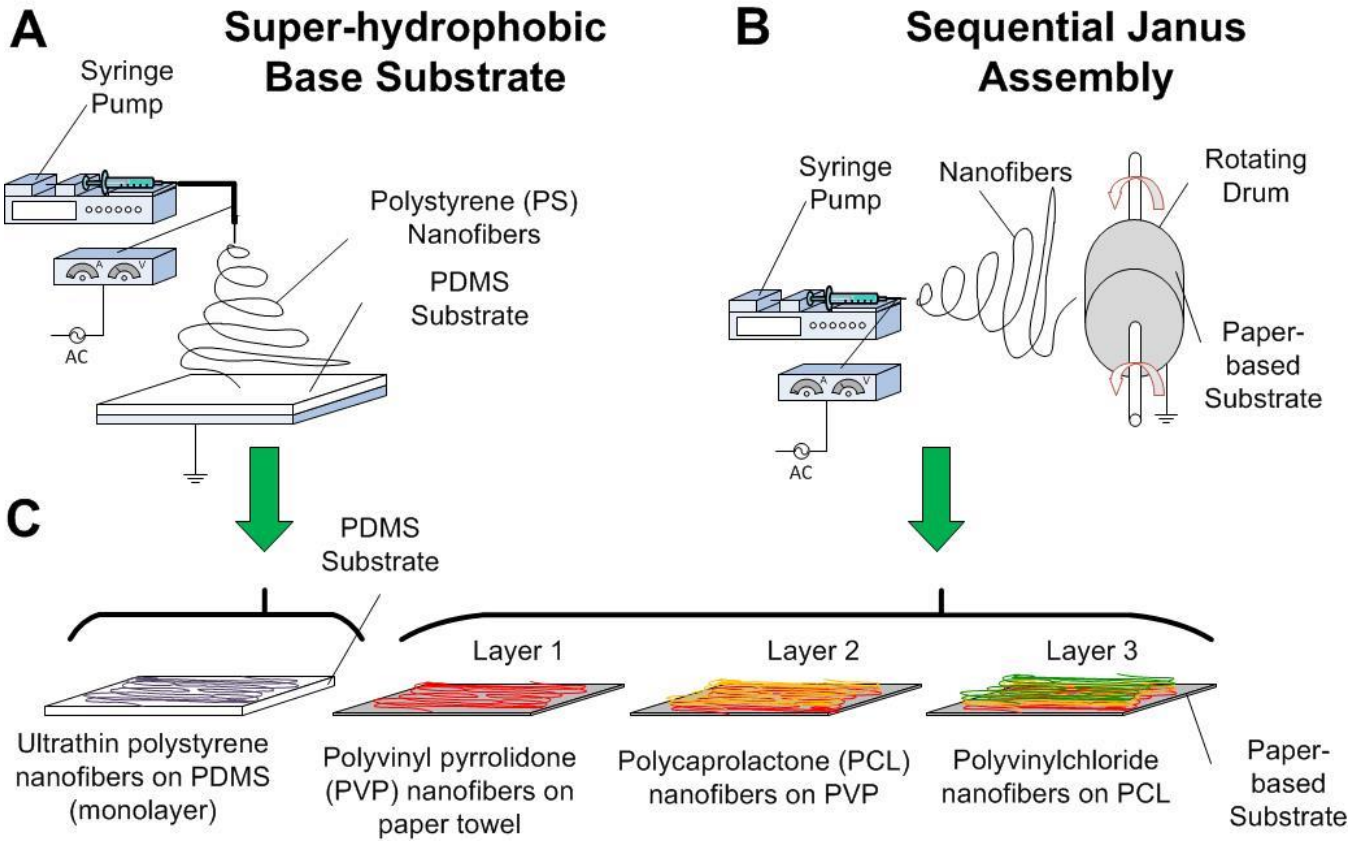

fig. S1. Synthesis of nanostructured Janus bilayer by sequential electrospinning. The systems is made of nanofiber layers of (**A**) superhydrophobic polystyrene on a PDMS substrate and (**B-C**) Janus bilayer stack comprising a sacrificial polyvinyl pyrrolidone (PVP), a hemi-wicking polycaprolactone (PCL) and a superhydrophobic polyvinyl chloride (PVC) layer on a paper substrate.

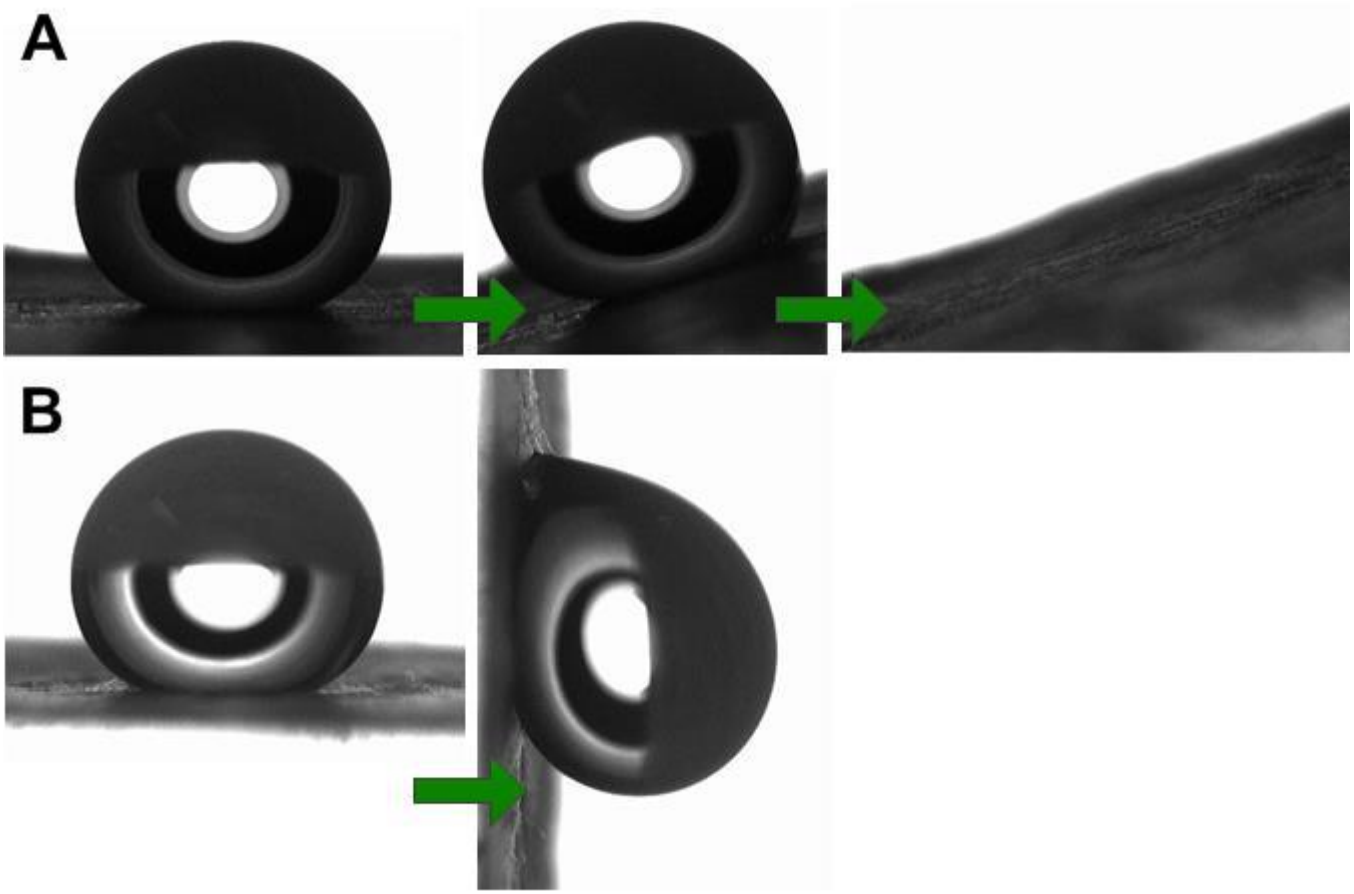

fig. S2. SA analysis of the superhydrophobic layers. (**A**) Lotus superhydrophobic polystyrene nanofiber layer and (**B**) pinning superhydrophobic polyvinyl chloride layer.

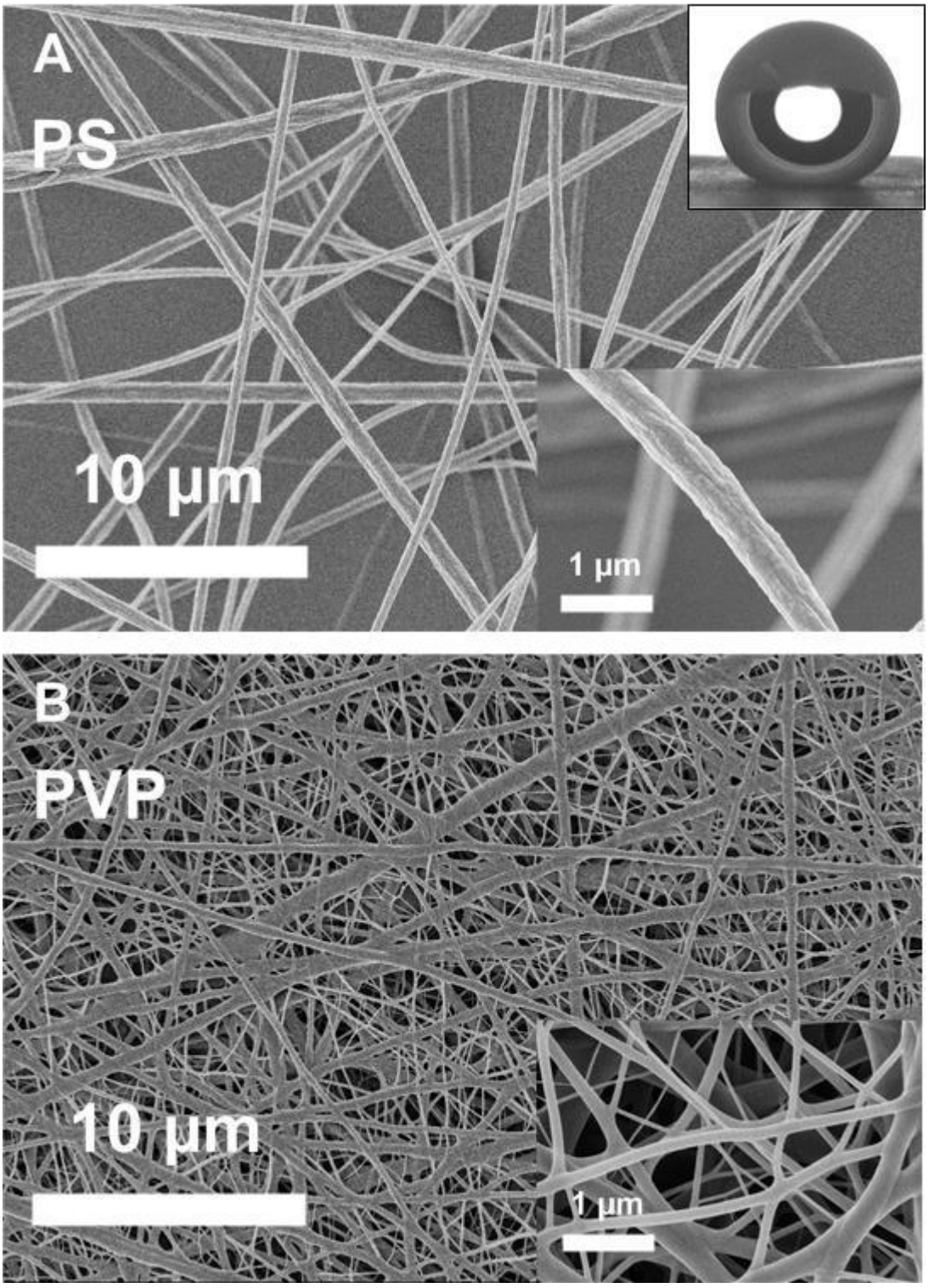

fig. S3. Morphological characterization (SEM) of the supporting and sacrificial layers. Nanofibrous (**A**) polystyrene as the dewetting platform and (**B**) polyvinyl pyrrolidone as the hygroscopic protective sacrificial layer.

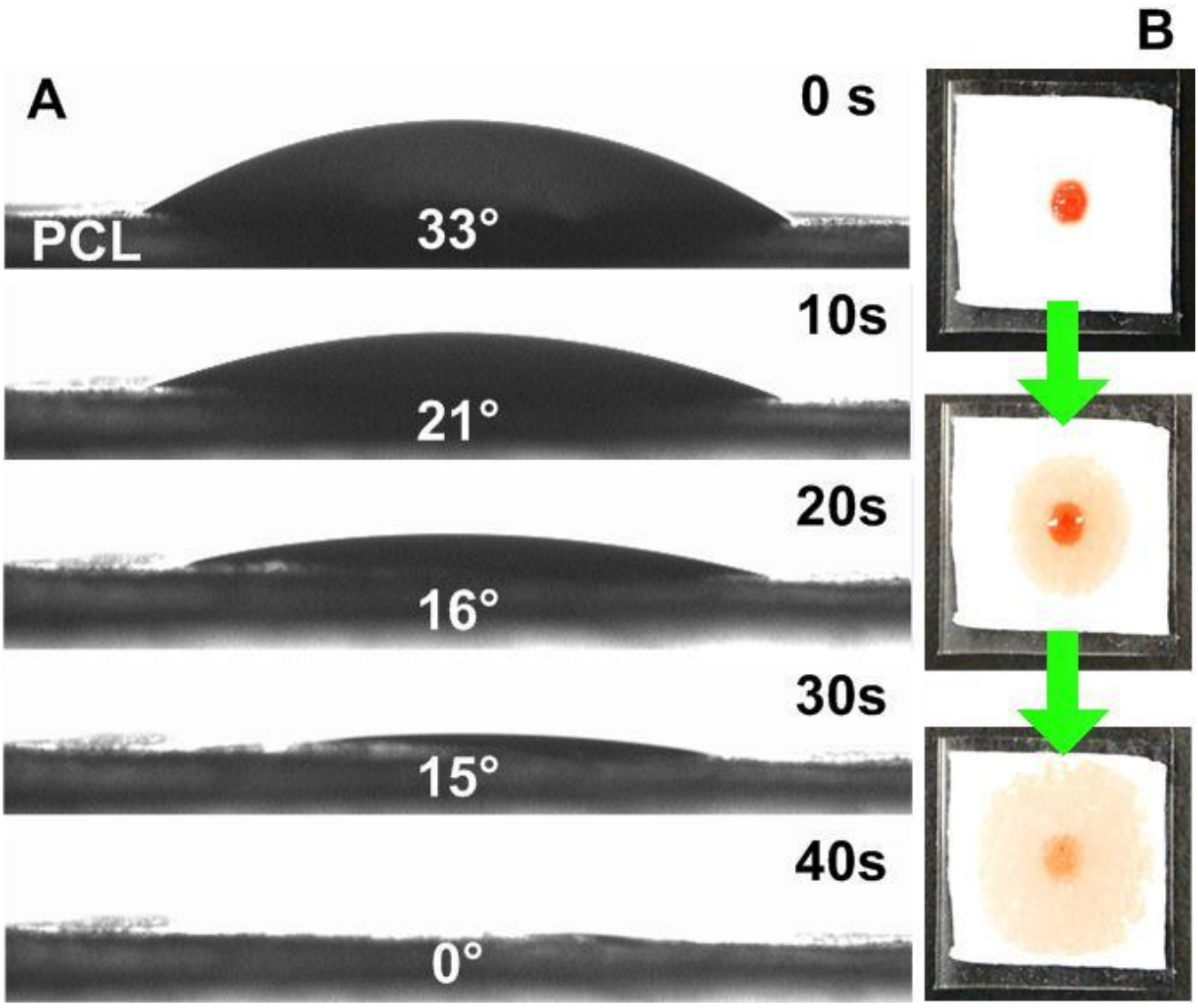

fig. S4. Hemiwicking superhydrophilic nature of the PCL layer. (**A**) Side-profile and (**B**) top-profile of the droplet wicking dynamics into a PCL monolayer.

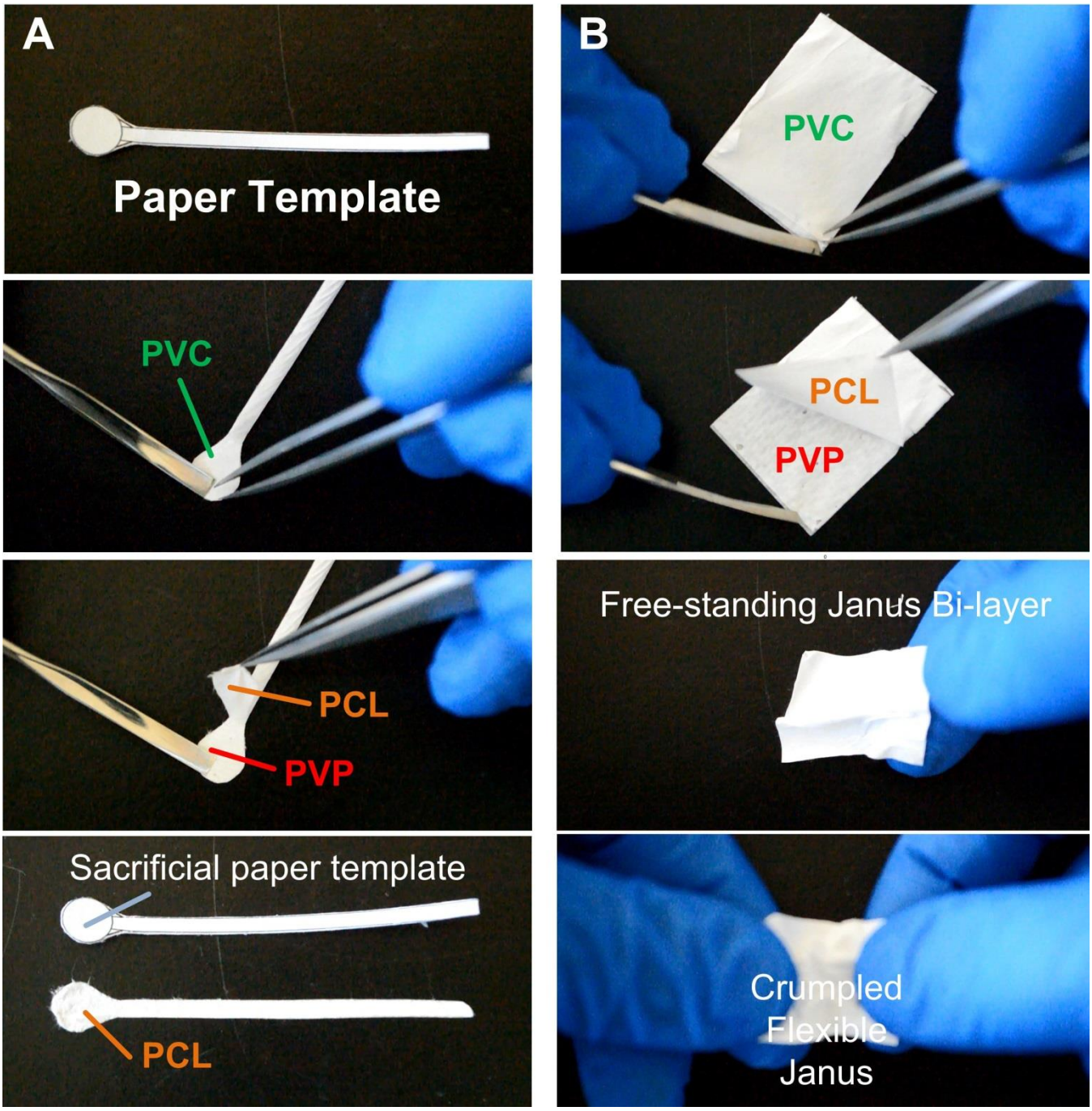

fig. S5. Separation of the Janus bilayer from the PVP protective layer. (**A**) Separation of the functional Janus bilayer template geometry. (**B**) Separation and manipulation of a rectangular-shaped free-standing Janus bilayer.

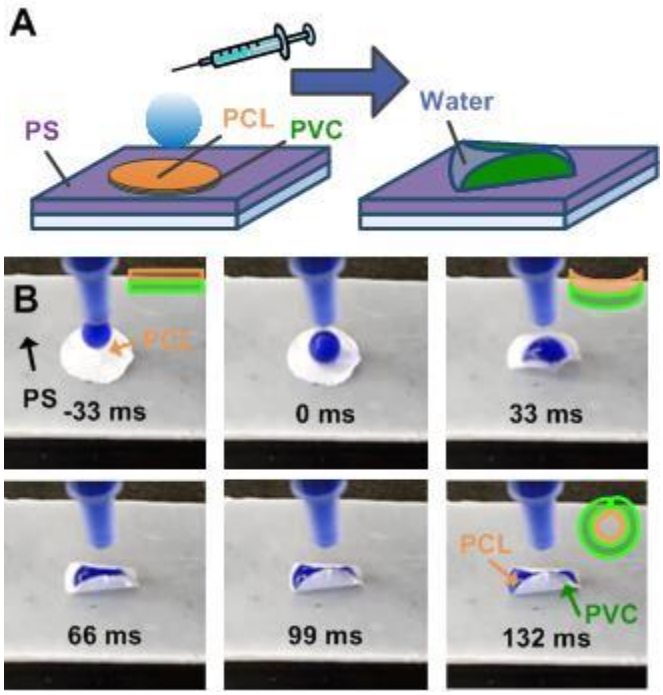

fig. S6. Static self-assembly of Janus bilayers. (**A**) Schematic illustration of the static self-assembly of the Janus bilayer in response to a water droplet. (**B**) Static self-assembly dynamics shown as a frame-by-frame analysis. The initial Janus bilayer response time was ≤ 33ms from droplet contact with the PCL surface.

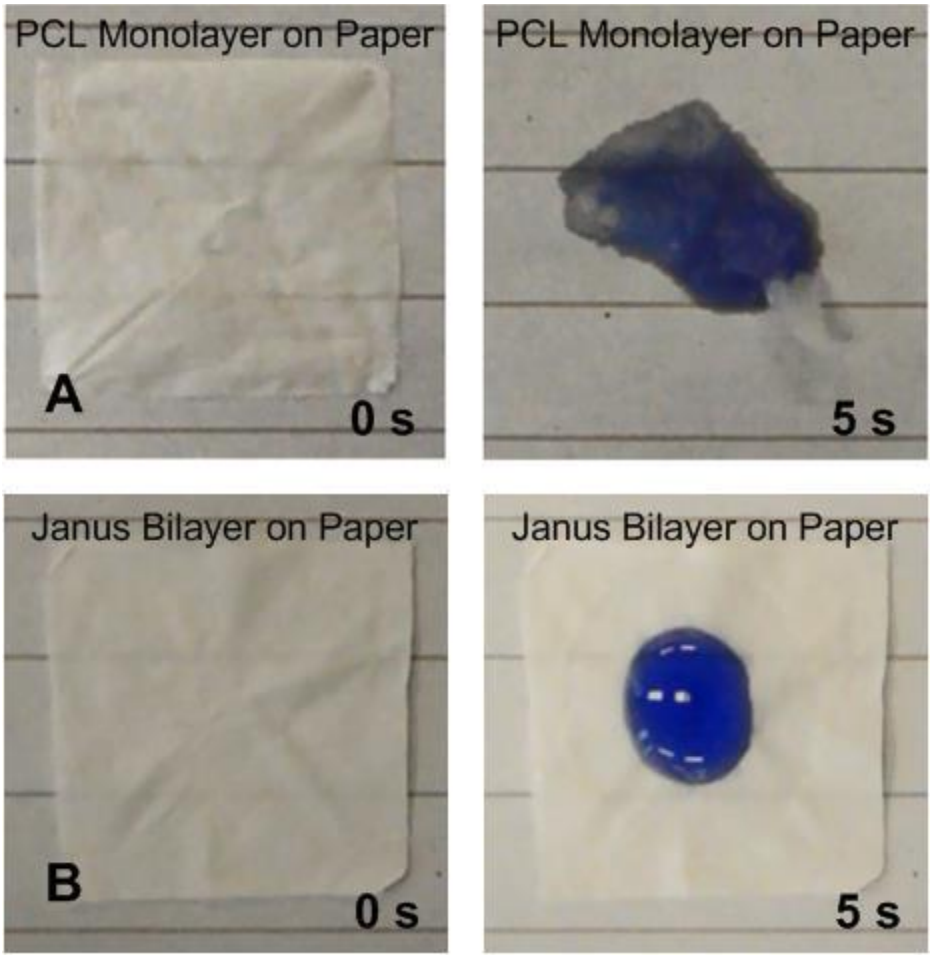

fig. S7. Janus bilayer and PCL monolayer response on hydrophilic (paper) substrates. (**A**) Monolayer with wet-through failure albeit rapid folding-wrinkling and (**B**) Janus bilayer with droplet holding capabilities showcasing a characteristic hemi-wicking droplet spreading.

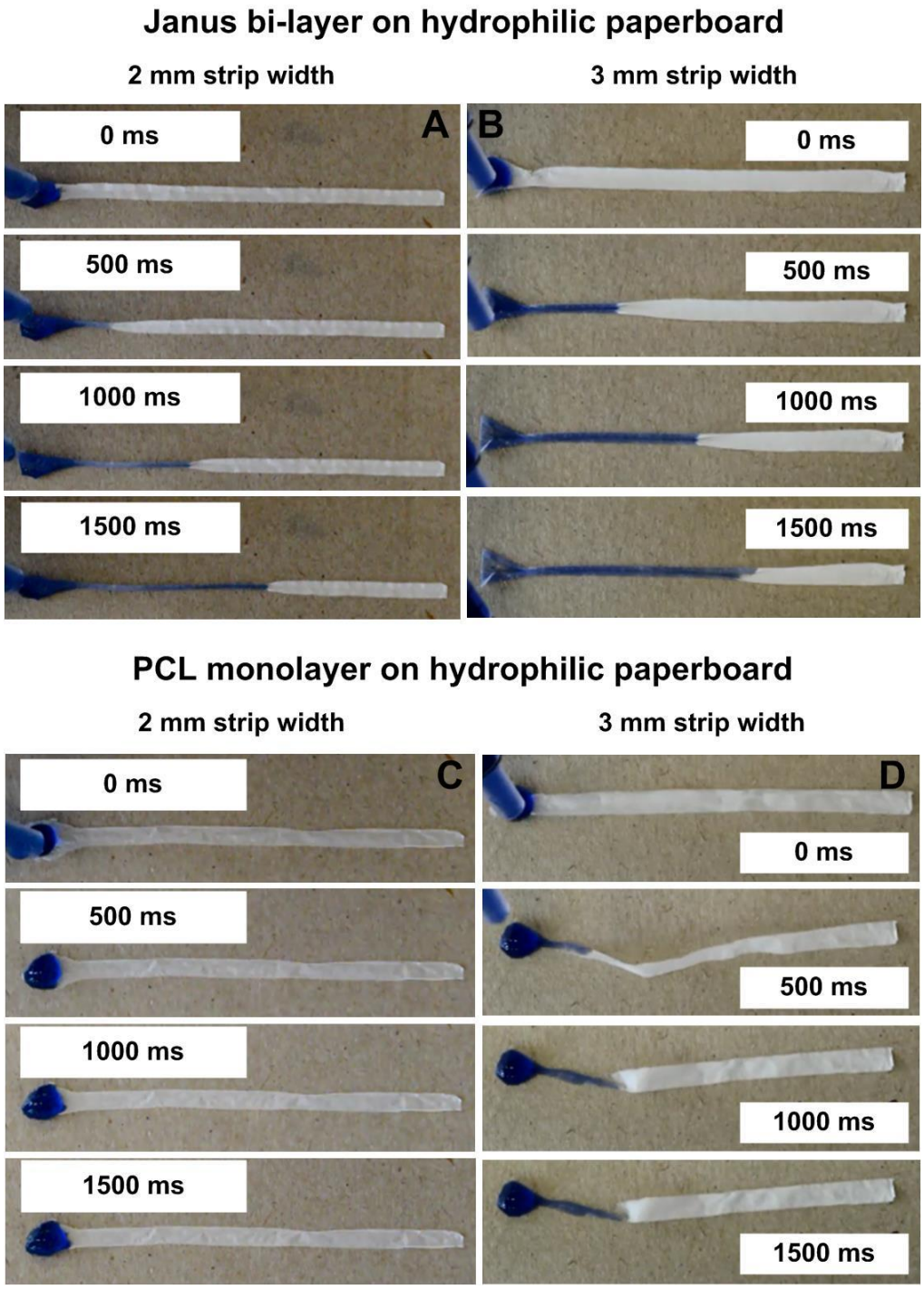

fig. S8. Qualitative wetting characterization of 2- and 3-mm strips of Janus bilayer and PCL monolayer on hydrophilic paperboard. (**A**-**B**) Janus bilayer with functionality at 2 and 3 mm widths respectively (albeit slower than on superhydrophobic PDMS-PS substrates) and (**C**-**D**) PCL monolayer with wetting failure at 2 and 3 mm widths, respectively.

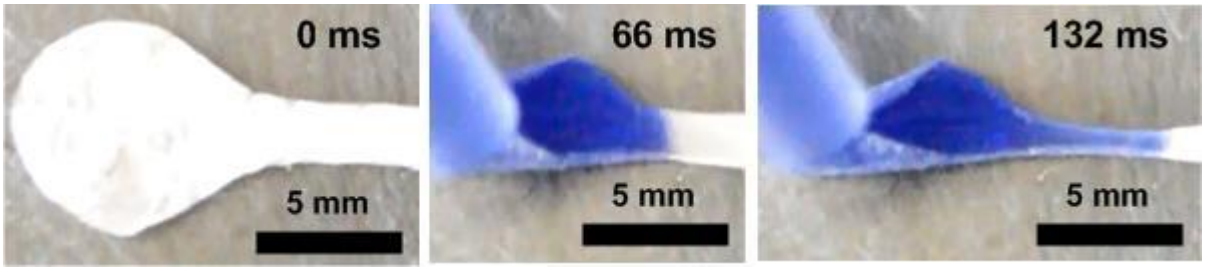

fig. S9. Enlarged images of initial Janus bilayer folding. The fluid transfer from bulb to the rectangular strip, revealing the formation of a quasi-cylindrical channel within 132 ms**.**

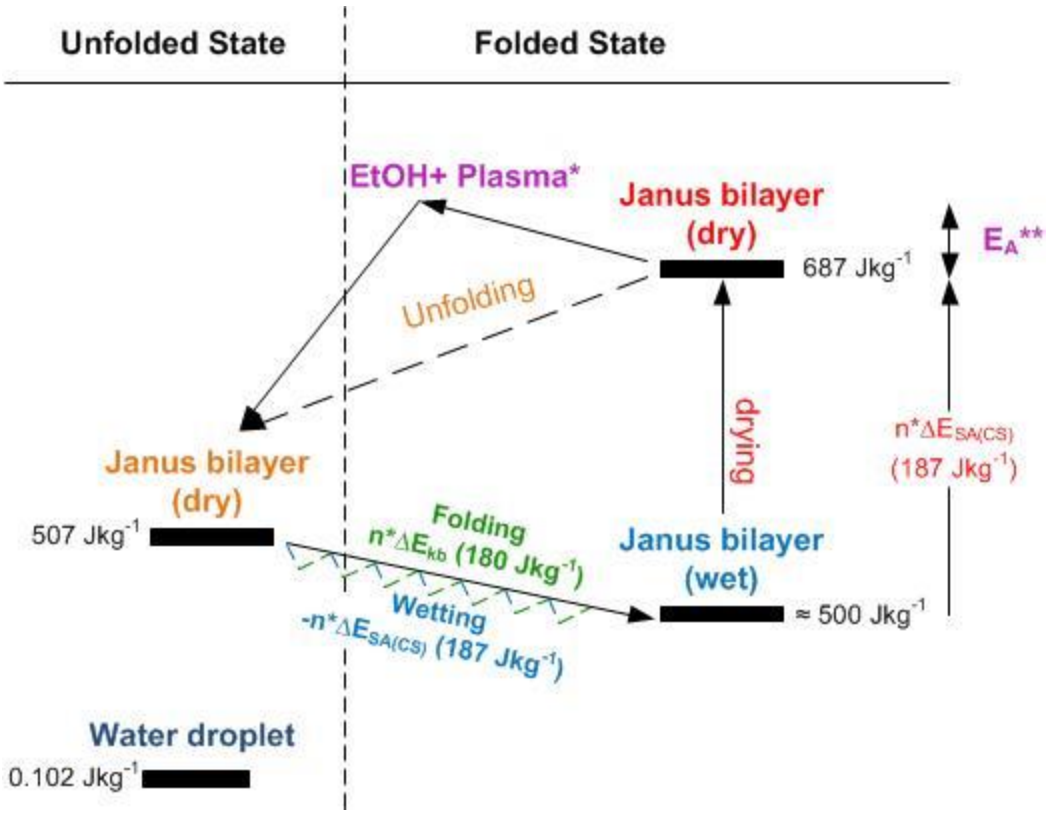

fig. S10. Representative thermodynamic states of the Janus bilayer during self-assembly. Wetting of the highly energetic dry-surface of the Janus bilayer (507 Jkg^{-1}) leads to a cascade (Mimosa Origami) of folding states (n) ultimately resulting in the folding of the whole Janus bi-layer length. The drop in surface energy ($\Delta E_{SA(CS)}$) is efficiently converted in elastic energy by the folding of each cross-sections ($\Delta E_{SA(CS)}$). The total energy density gain during wetting is estimated to 187 Jkg^{-1} and the elastic energy gain is estimated to 180 Jkg^{-1}. Drying of the folded Janus bi-layer results in the highest energy state (687 Jkg^{-1}) due to the contribution of the elastic energy ($n^*\Delta E_{kb}$). Immersion in the ethanol* bath supplies the activation energy (E_A**) to start the unfolding while plasma* treatment restores the initial surface energy enabling a new self-assembly cycle. Equations S8-9 were used for the computation of the surface energy (γ_{SV} and γ_{SL}) of the dry and wetted Janus bilayer.

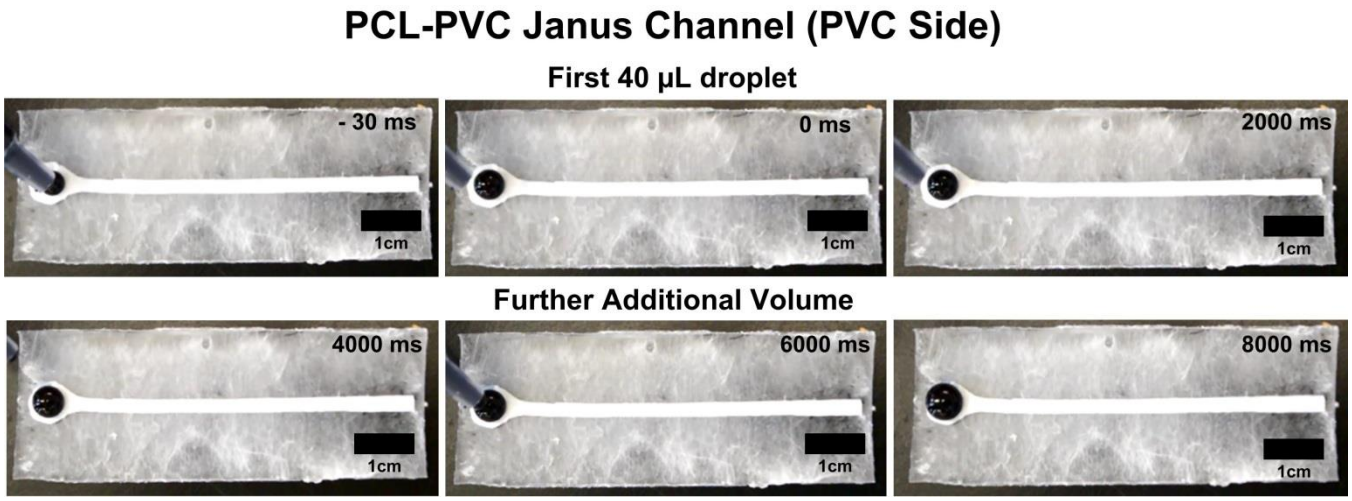

fig. S11. Response of the PVC side of the Janus bilayer to water. The wetting characterization of the opposing superhydrophobic PVC side of a 2 mm-wide strip of Janus bilayer on superhydrophobic nanofibrous substrates reveals no Mimosa Origami self-assembly.

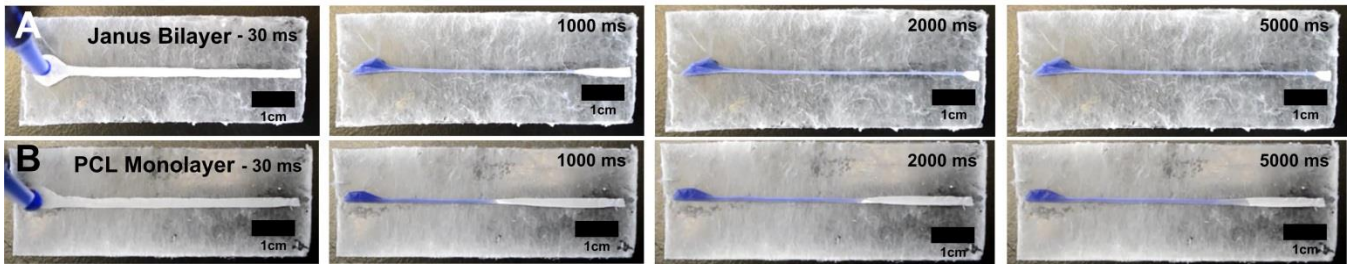

fig. S12. Mimosa Origami of a 2-mm strip of Janus bilayer and PCL monolayer on the PDMS-PS substrates. (**A**) Janus bilayer with full functionality and (**B**) PCL monolayer with suboptimal functionality due to wet-through failure.

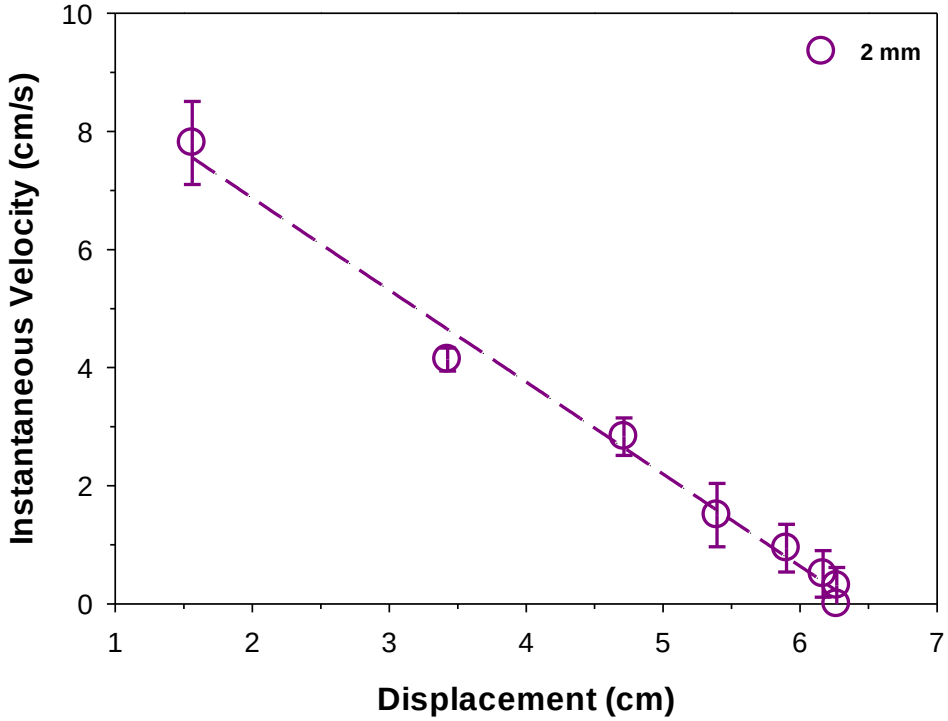

fig. S13. Decreasing stimulus propagation rate for a 2-mm-wide strip and a stimulus droplet size of 40 µl.

Captions for movies S1 to S9:

movie S1. Static self-assembling properties of circular shaped Janus bilayer demonstrating artificial tropism in response to a microdroplet. Bilayer was laid onto a superhydrophobic PS-PDMS substrate for this experiment. Video was slowed down 8X.

movie S2. Mimosa Origami assembly of the Janus bilayer strips on a superhydrophobic PS-PDMS substrate. Strip had a width of 2 mm. Actuation was performed using a 40 µL droplet.

movie S3. Mimosa Origami assembly of the Janus bilayer strips performing double right angle turns on superhydrophobic PS-PDMS substrate. Additional supply of water was notably able to help overcome actuation across corners, while extending actuation distance.

movie S4. Mimosa Origami assembly of the Janus bilayer strips performing longer and tighter double right angle turns on superhydrophobic PS-PDMS substrate. Additional supply of water was notably able to help overcome actuation across corners, while extending actuation distance.

movie S5. Mimosa Origami assembly of the Janus bilayer strips on a superhydrophobic PS-PDMS substrate. Strip had a width of 4 mm. Actuation was performed using a 40 µL droplet.

movie S6. Modular microfluidics: Janus-based Mimosa Origami strips with double-ended bulbs on a superhydrophobic PS-PDMS substrate showing in-channel droplet mixing. Actuation was performed using two 40 µL droplet.

movie S7. Modular microfluidics: Janus-based Mimosa Origami strips with double-ended bulbs with a central bulb on a superhydrophobic PS-PDMS substrate showing in-bulb droplet mixing. Actuation was performed using two 40 µL droplet.

movie S8. Modular microfluidics: Janus-based Mimosa Origami strips at a T-junction, showcasing double-ended split for potential in multi-channel capabilities. Motion was notably slowed at the T-junction, in a similar fashion to right-angled turns. Actuation was performed using a 40 µL droplet.

movie S9. Cyclic insertion and removal of water from an as-assembled microfluidics channel, showcasing suitability towards pump-aided microfluidic designs.